INTERNATIONAL JOURNAL FOR NUMERICAL METHODS IN FLUIDS
Int. J. Numer. Meth. Fluids 2009; **00**:1–6 *Prepared using* fldauth.cls *[Version: 2002/09/18 v1.01]*

Coupled Fluid-Solid Interaction Under Shock Wave Loading: Part II – Dynamic Interfaces

D. Gregory Tipton[1*] , Mark A. Christon[2], Marc S. Ingber[3]

[1] *Sandia National Laboratories, Albuquerque, New Mexico*
[2] *CTO Office, Dassault Systèmes SIMULIA, Providence, Rhode Island*
[3] *Department of Mechanical Engineering, University of New Mexico, Albuquerque, New Mexico*

SUMMARY

This paper is the second of two that consider the treatment of fluid-solid interaction problems where the solid experiences wave loading and large bulk Lagrangian displacements. In part-I, we presented the formulation for the edge-based unstructured-grid Euler solver in the context of a discontinuous-Galerkin framework with the extensions used to treat internal fluid-solid interfaces. A super-sampled $\mathcal{L}^2$ projection was used to construct level-set data from the Lagrangian interface, and a narrow-band approach was used to identify and construct appropriate ghost data and boundary conditions at the fluid-solid interface. A series of benchmark problems were used to verify the treatment of the fluid-solid interface conditions with a static interface position. In this paper, we consider the treatment of dynamic interfaces and the associated large bulk Lagrangian displacements of the solid. We present the coupled dynamic fluid-solid system, and develop an explicit, monolithic treatment of the fully-coupled system. The conditions associated with moving interfaces and their implementation are discussed. A comparison of moving vs. fixed reference frames is used to verify the dynamic interface treatment. Finally, a series of two and and three-dimensional projectile and shock-body interaction calculations are presented. Ultimately, the use of the Lagrangian interface position and a super-sampled projection for fast level-set construction, the narrow-band extraction of ghost data, and monolithic explicit solution algorithm has proved to be a computationally efficient means for treating shock induced fluid-solid interaction problems.

KEY WORDS: Fluid-solid interaction; Euler equations; level-set; discontinuous Galerkin; shock loading; Riemann problem; interface conditions; super-sampled projection

1. INTRODUCTION

This paper is the second of two that consider the treatment of fluid-solid interaction problems under shock wave loading using overlapping, unstructured grids. The focus for this work is on the class of problems where the fluid-solid interaction is characterized by shock wave loading that results in a large bulk Lagrangian displacement of the solid. Examples of this class of FSI

---

[*] Correspondence to: D. Gregory Tipton, Sandia National Laboratories, Albuquerque, NM. Email: dgtipto@sandia.gov

Received 15 July 2009
Revised xxxxxx
Accepted xxxxxx

problem include shock wave loading from an explosive blast, and the interaction of a ballistic object with an incident shock.

The overall goal for this research is to develop computational methods for simulating fluid-solid interaction problems on overlapping, unstructured meshes. The use of overlapping meshes accommodates large relative motions between the fluid and solid fields that are not easily accommodated by remesh/remap strategies. A key component of this work has been the development of methods to accurately and efficiently identify the fluid-solid interface on the fluid mesh and enforce the appropriate boundary conditions.

In part-I an edge-based discontinuous Galerkin method, with extensions to treat internal boundaries and cut edges, was used to solve the Euler equations on unstructured grids. A new super-sampled projection method was used to initialize a level-set function to identify the fluid-solid interface on the Eulerian fluid grid. A variant of the ghost-fluid method was then used to enforce the interface conditions at the edges of the fluid grid cut by the interface. The focus for the current work is on the development of a monolithic, explicit algorithm for the treatment of the fully-coupled FSI system. The methods for imposing the interface conditions developed in part-I [6] are extended to moving interfaces.

The ensuing discussion begins with the formulation of the coupled fluid-solid system. A six degree-of-freedom rigid body description is used for the solid body. The coupling terms at the wetted interface are presented, and an explicit monolithic time integration scheme for the coupled fluid-solid system is developed using a Runge-Kutta time integrator. The treatment of the dynamic interface is then discussed. The issues of uncovering conditions for the fluid and construction of numerical fluxes are considered. In §4, rigid-body translation at the convective velocity is used as a verification test for the numerical implementation of the interface conditions. This is followed by a more detailed comparison between the flow computed in a fixed Eulerian frame with prescribed velocity, and the flow computed using a stationary fluid and rigid-body moving at with the same velocity. In §5 a series of projectile calculations are presented, followed by concluding remarks.

2. FORMULATION

This section presents the system of equations for an inviscid, compressible fluid coupled to a rigid body. The fluid-solid system is shown in Figure 1 where the fluid domain is Ω_F, with boundary Γ_F, the solid domain is Ω_S, with boundary Γ_S, and the fluid-solid interface is denoted as, Γ_{FS}. We note in passing that, the use of a rigid body poses few restrictions, and the extension to a fully-elastic body is relatively straight-forward.

2.1. Compressible Fluid Dynamics

The Euler equations in flux divergence form are

$$\frac{\partial \mathbf{U}}{\partial t} + \nabla \cdot \mathbf{F}(\mathbf{U}) = 0 \tag{1}$$

where $\mathbf{U} = [\rho \ \rho u \ \rho v \ \rho w \ E]^T$ is the vector of conserved variables, the vector of primitive variables is $\mathbf{W} = [\rho \ u \ v \ w \ p]^T$, and $\mathbf{F}(\mathbf{U})$ is the vector of physical fluxes as presented in [6].

An equation-of-state is required to close the system of conservation laws in equation 1. For the purposes of this discussion we use a γ-law gas equation-of-state, $p = (\gamma - 1)\rho e$, where e

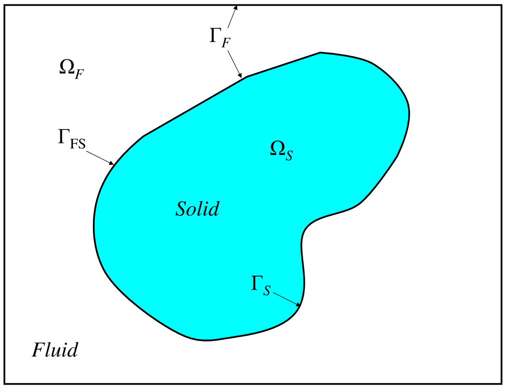

Figure 1. Definitions of the fluid and solid domains and boundaries.

is the specific internal energy. However, this does not pose a restriction on the formulation or solution method. The details of the edge-based unstructured-grid Euler solver used here are presented in part-I [6] of this work.

2.2. Rigid-Body Dynamics

Rigid bodies occupy space and may undergo both translation and rotation in a dynamic sense. To describe the translation of a rigid body in an inertial (Eulerian) reference frame, the location of the center-of-mass, $\mathbf{x}_{cm}(t)$, is tracked over time. To describe the body's rotation about the center-of-mass, a quaternion, $\mathbf{q}(t)$, is used in lieu of a rotation tensor, $\mathbf{R}(t)$ [1, 2]. In three spatial dimensions, the quaternion is four-dimensional and is represented as

$$\mathbf{q}(t) = s(t) + v_x(t)\mathbf{i} + v_y(t)\mathbf{j} + v_z(t)\mathbf{k}, \tag{2}$$

where s, v_x, v_y, and v_z are commonly referred to as Euler parameters. Here, we choose to use quaternions for our rotational degrees-of-freedom because they do not suffer from the limitations of a rotation tensor, i.e., "gimbal lock" and loss of accuracy over time. Together, $\mathbf{x}_{cm}(t)$ and $\mathbf{q}(t)$ constitute the variables required to describe the position and orientation of a rigid body in an inertial reference frame.

To describe the shape of the rigid body, it is convenient to use a body coordinate (Lagrangian) system that is attached to the center-of-mass and rotates/translates with it. The inertial and body coordinate systems are shown in Figure 2. Here, the initial location of the body is $\mathbf{x}_{cm}(0)$. At time t, the rigid body has translated to $\mathbf{x}_{cm}(t)$ and experienced a finite rotation described by $\mathbf{q}(t)$.

The location of a point on the body, $\mathbf{p}(t)$, may be calculated by rotating the point $\mathbf{p}(0)$ into the proper coordinate system at time t, and translating the point with the rigid body. It should be noted that a rotation tensor, $\mathbf{R}(t)$, can be derived from the components of the quaternion at any time, t. The location of a point on the body can be calculated as

$$\mathbf{p}(t) = \mathbf{R}(t)\mathbf{p}(0) + \mathbf{x}_{cm}(t). \tag{3}$$

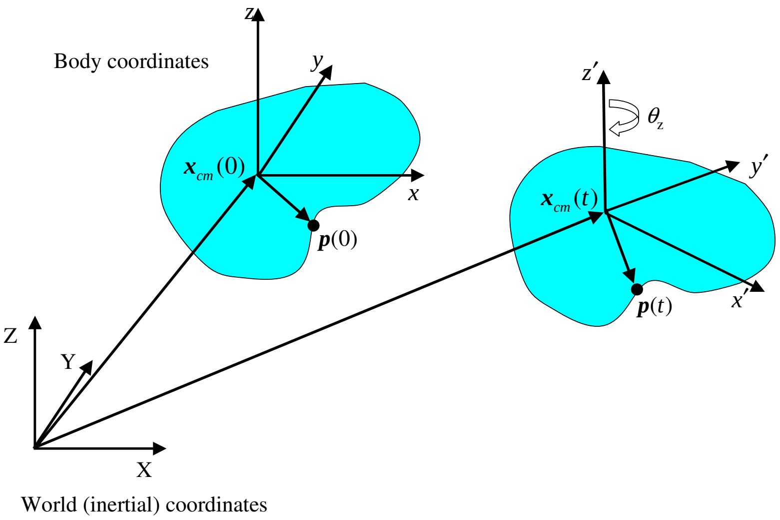

Figure 2. Inertial and body coordinate systems. Position and orientation of the body are described with respect to the inertial coordinate system.

The velocity of the rigid body's center-of-mass is

$$\mathbf{v}_{cm} = \frac{d\mathbf{x}_{cm}}{dt} \tag{4}$$

The angular velocity, $\boldsymbol{\omega}$, describes the rate at which the rigid body spins about its center-of-mass. The direction of $\boldsymbol{\omega}$ defines the axis for rotation, and $\|\boldsymbol{\omega}\|$ defines the rotational speed.

The instantaneous velocity of a given point on the rigid body is written in terms of the velocity of the center-of-mass and the angular velocity as

$$\begin{aligned}\mathbf{v}_p(t) &= \boldsymbol{\omega} \times \{\mathbf{p}(t) - \mathbf{x}_{cm}(t)\} + \mathbf{v}_{cm}(t) \\ &= \boldsymbol{\omega} \times \{\mathbf{R}(t)\mathbf{p}(0)\} + \mathbf{v}_{cm}(t).\end{aligned} \tag{5}$$

This relationship is shown graphically in Figure 3.

There is a linear relationship between the velocity and time-derivative of the position vector, i.e., $\mathbf{v}_{cm} = \dot{\mathbf{x}}_{cm}$. There is a similar relationship for the rotation,

$$\dot{\mathbf{q}}(t) = \frac{1}{2}\boldsymbol{\omega}(t)\mathbf{q}(t). \tag{6}$$

The net force on a rigid body, $\mathbf{f}(t)$, is simply the sum of all the external forces applied. The applied moments or torque may be computed in terms of the applied forces at a given point as

$$\mathbf{T}(t) = \{\mathbf{p}(t) - \mathbf{x}_{cm}(t)\} \times \mathbf{f}(t) \tag{7}$$

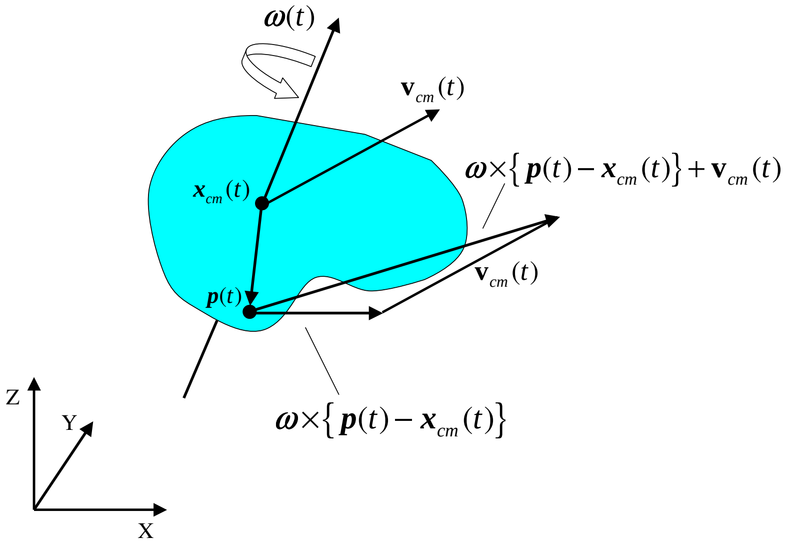

Figure 3. Linear and angular velocity components used in the computation of the velocity at a point.

The linear momentum of a rigid body is given as

$$\mathbf{P}(t) = m\mathbf{v}_{cm}(t) \tag{8}$$

where m is the mass of the body and $\mathbf{v}_{cm}(t)$ is the velocity of the body at time t.

The conservation of linear momentum is given by

$$\frac{d\mathbf{P}}{dt} = m\frac{d\mathbf{v}_{cm}}{dt} = \mathbf{f}(t), \tag{9}$$

where $\mathbf{f}$ represents the net external forces acting on the body.

Similarly, the angular momentum of a rigid body is defined as

$$\mathbf{L} = \mathbf{I}\boldsymbol{\omega}, \tag{10}$$

where $\mathbf{I}$ is the inertia tensor about the center-of-mass and $\boldsymbol{\omega}$ is the angular velocity of the body. Conservation of angular momentum may be written as

$$\frac{d\mathbf{L}}{dt} = \mathbf{T}(t), \tag{11}$$

where $\mathbf{T}$ represents the net external moments (or torque) acting on the body.

The state of a rigid body at any given time, t, is completely defined by its position $\mathbf{x}(t)$, its orientation described by $\mathbf{q}(t)$, its linear momentum $\mathbf{P}(t)$, and its angular momentum $\mathbf{L}(t)$ [2]. For simplicity, the subscript cm has been dropped from the position and velocity vectors.

These quantities can be written in terms of a state vector, $\mathbf{Y}$, for the body as

$$\mathbf{Y}(t) = \left\{ \begin{array}{c} \mathbf{x}(t) \\ \mathbf{q}(t) \\ \mathbf{P}(t) \\ \mathbf{L}(t) \end{array} \right\}. \tag{12}$$

Thus, $\mathbf{Y}(t)$ is a vector with thirteen components (three for position $\mathbf{x}(t)$, four for the quaternion $\mathbf{q}(t)$, three for the linear momentum $\mathbf{P}(t)$, and three for the angular momentum $\mathbf{L}(t)$).

The motion of the rigid body is completely described by the evolution of this state vector over time. Thus, the rigid-body equations of motion can be represented by a first–order system in time as follows,

$$\frac{d}{dt}\mathbf{Y}(t) = \frac{d}{dt} \left\{ \begin{array}{c} \mathbf{x}(t) \\ \mathbf{q}(t) \\ \mathbf{P}(t) \\ \mathbf{L}(t) \end{array} \right\} = \left\{ \begin{array}{c} \mathbf{v}(t) \\ \frac{1}{2}\boldsymbol{\omega}(t)\mathbf{q}(t) \\ \mathbf{f}(t) \\ \mathbf{T}(t) \end{array} \right\}. \tag{13}$$

Equipped with the necessary initial conditions, Equation 13 can be integrated term-by-term to obtain the state of the rigid body at any time, t.

2.3. Interface conditions

On the fluid-solid interface, Γ_{FS}, kinematic constraints require compatibility between the fluid velocity and the solid velocity in the normal direction, i.e,

$$\mathbf{u}_F^i \cdot \mathbf{n}_i = \mathbf{u}_S^i \cdot \mathbf{n}_i. \tag{14}$$

Here, $\mathbf{u}_F^i$ is the velocity of the fluid at the interface, $\mathbf{u}_S^i$ is the velocity of the solid body at the interface, and $\mathbf{n}_i$ is the unit normal at the interface directed outward from the solid. The velocity at any point on the interface can be computed from the rigid-body translational and rotational velocities as

$$\mathbf{u}_S^i = \boldsymbol{\omega} \times (\mathbf{p}(t) - \mathbf{x}(t)) + \mathbf{v}, \tag{15}$$

where the vector $\mathbf{p}(t) - \mathbf{x}(t)$ is the moment arm from the center-of-mass to the point on the interface (see Figure 3).

Also on the interface, Γ_{FS}, the fluid pressure will exert a resultant force and moment on the body. The rigid-body forces and moments can be calculated from the fluid pressure as

$$\mathbf{f} = \oint_{\Gamma_{FS}} p\mathbf{n}_i d\Gamma_{FS} \tag{16}$$

$$\mathbf{T} = \oint_{\Gamma_{FS}} p\mathbf{n}_i \times \mathbf{r} d\Gamma_{FS}, \tag{17}$$

where $\mathbf{n}_i$ is the outward normal to the solid at the interface, and $\mathbf{r}$ is the moment arm from the center-of-mass of the body to a point on the interface.

2.4. Coupled System

The complete system of equations is given as

$$\frac{\partial \mathbf{U}}{\partial t} + \nabla \cdot \mathbf{F}(\mathbf{U}) = 0 \quad \text{in } \Omega_F, \tag{18}$$

$$\frac{d\mathbf{Y}}{dt} = \mathbf{F}_{RB} \quad \text{in } \Omega_S, \tag{19}$$

$$\mathbf{u}_F^i \cdot \mathbf{n}_i = \mathbf{u}_S^i \cdot \mathbf{n}_i \quad \text{on } \Gamma_{FS}, \tag{20}$$

$$\mathbf{f} = \oint_{\Gamma_{FS}} p\mathbf{n}_i d\Gamma_{FS} \quad \text{on } \Gamma_{FS}, \tag{21}$$

$$\mathbf{T} = \oint_{\Gamma_{FS}} p\mathbf{n}_i \times \mathbf{r} d\Gamma_{FS} \quad \text{on } \Gamma_{FS}. \tag{22}$$

2.5. Time Integration with Dynamic Interfaces

The semi-discrete the Euler equations can be written as the first-order system of equations

$$\frac{d\mathbf{U}(t)}{dt} = -\mathcal{F}(\mathbf{U}(t)) \tag{23}$$

where $\mathcal{F}(\mathbf{U}(t))$ is the discrete operator for the numerical flux function. (See part-I [6] for additional details.) The rigid-body equations of motion presented in equation 13, can also be represented as a first-order system of equations

$$\frac{d\mathbf{Y}(t)}{dt} = \mathbf{F}(t) \tag{24}$$

where $\mathbf{F}(t)$ is a function of the applied forces and moments on the body. Both sets of equations can be combined into the single system of equations

$$\frac{d}{dt}\left\{ \begin{array}{c} \mathbf{U}(t) \\ \mathbf{Y}(t) \end{array} \right\} = -\left\{ \begin{array}{c} \mathcal{F}(\mathbf{U}(t)) \\ -\mathbf{F}(t) \end{array} \right\}. \tag{25}$$

Equation 25 represents a fully-coupled system of equations with the coupling terms contained in the right-hand-side. Velocities at the fluid-solid interface are enforced on the fluid by appropriately setting terms in the flux function, $\mathcal{F}(\mathbf{U}(t))$. Similarly, the forces and moments on the rigid body due to the fluid pressure are contained in $\mathbf{F}(t)$. All of these coupling terms can be calculated at the beginning of any given time step. Thus, the complete system can be integrated as one monolithic system of equations.

Given the first-order coupled systems, several explicit integration methods were considered. The first-order forward Euler integration scheme is given as

$$\mathbf{V}^{n+1} = \mathbf{V}^n - \Delta t \mathcal{L}(\mathbf{V}^n). \tag{26}$$

Here, $\mathbf{V} = [\mathbf{U}(t), \mathbf{Y}(t)]^T$ is the vector of unknowns and, $\mathcal{L}(V)$ is the complete discrete operator for the right-hand-side of equation 25.

In addition to forward Euler, the strong stability preserving (SSP) Runge-Kutta integration scheme [3, 4] was also implemented. The second-order, two-stage SSP Runge-Kutta integration scheme for the coupled system is

$$\mathbf{V}^{(1)} = \mathbf{V}^n - \Delta t \mathcal{L}(\mathbf{V}^n) \tag{27}$$

$$\mathbf{V}^{n+1} = \frac{1}{2}\mathbf{V}^n + \frac{1}{2}\mathbf{V}^{(1)} - \frac{1}{2}\Delta t \mathcal{L}(\mathbf{V}^{(1)}). \tag{28}$$

The SSP Runge-Kutta integrator was used for all the example problems presented here.

The rigid-body equations of motion presented in equations 24 and 25 capture both translational and rotational motion. Position, orientation, and momentum of the rigid body are represented in the state vector, $\mathbf{Y}$ (see equation 13). For the work presented here, only translational motion was required for the analytic interfaces. In this situation, linear momentum changes due to fluid pressure acting on the interface were not taken into account. In this limit, the equations of motion for the rigid interfaces reduces to

$$\frac{d\mathbf{x}(t)}{dt} = \mathbf{v}(t) \tag{29}$$

where $\mathbf{x}(t)$ is the position of the rigid body's center-of-mass, and $\mathbf{v}(t)$ is the velocity of the rigid body.

3. DYNAMIC INTERFACE TREATMENT

The static interface treatment presented in part-I [6] is used as the starting point for the dynamic interface treatment. Here, the interface velocity must be accounted for in the interface conditions. In addition, special attention must be paid to the fluid conditions when ghost-elements are uncovered during a time step due to the motion of the solid body.

3.1. Uncovering Conditions

During the evolution of an FSI problem with a moving body, elements that are covered by the Lagrangian body at t^{n-1} may be uncovered at t^n. For the solution to proceed to t^{n+1}, initial data needs to specified in these newly uncovered elements for t^n (see equation 26 or 28). Unfortunately, the state in these elements was not computed during the previous time step ($t^{n-1} \rightarrow t^n$). Instead, ghost data was set in these elements to enforce the interface conditions,

$$\begin{gathered} \rho_g = \rho_s \\ \mathbf{u}_g \cdot \mathbf{n}_i = 2(\mathbf{u}_i \cdot \mathbf{n}_i) - \mathbf{u}_s \cdot \mathbf{n}_i \\ \mathbf{u}_g \cdot \mathbf{t}_i = \mathbf{u}_s \cdot \mathbf{t}_i \\ p_g = p_s, \end{gathered} \tag{30}$$

where $\mathbf{n}_i$ is the unit normal vector at the interface and $\mathbf{t}_i$ is the unit tangent vector. The subscripts s and g refer to the source data and the ghost data on either side of the cut edge.

This source data is saved as the initial fluid data for newly uncovered elements

$$\begin{gathered} \rho\left(t^n\right) = \rho_s\left(t^{n-1}\right) \\ \mathbf{u}\left(t^n\right) = \mathbf{u}_s\left(t^{n-1}\right) \\ p\left(t^n\right) = p_s\left(t^{n-1}\right). \end{gathered} \tag{31}$$

We refer to equation 31 as the uncovering conditions.

As an example, consider Figure 4(a). Ghost data is placed in the two ghost-cut elements to enforce boundary conditions at the interface at time t^{n-1}. As described in part-I, this ghost data is taken from a source point on each cut edge and used in the subsequent flux calculation

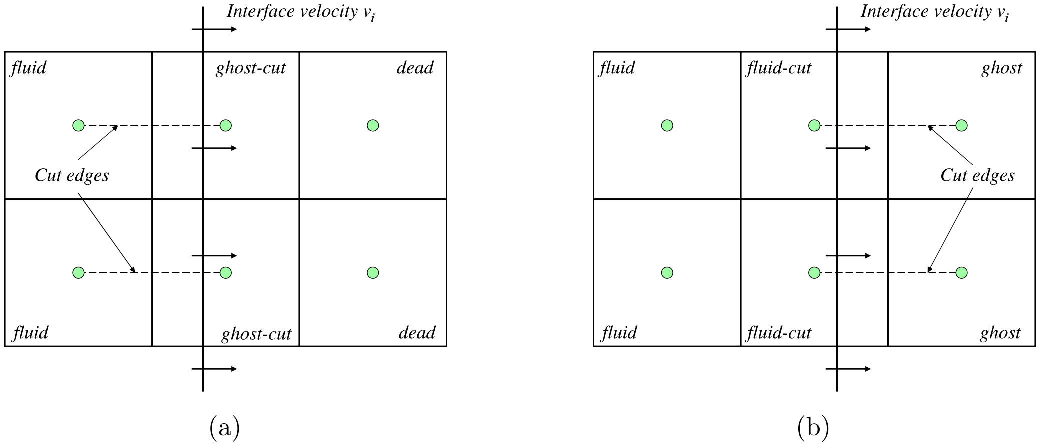

Figure 4. Example showing elements being uncovered by the interface during a time step. (a) The center elements are covered by the interface at time t^{n-1}. (b) The center elements are not covered by the interface at time t^n. Ghost data from time t^{n-1} is used as the initial data for these elements at time t^n.

for that edge. At time t^n, the interface has moved and these elements are now in the fluid (see Figure 4(b)). The source data $[\rho_s, \mathbf{u}_s, p_s]^T$ used at t^{n-1} is kept as the initial state data at t^n for the uncovered elements in accordance with equation 31.

It should be noted that both of the cut elements depicted in Figure 4 have only one cut edge. This may not be the case for arbitrarily oriented interfaces on an unstructured 3D grid. In general, a single element could have multiple cut edges. As an example, Figure 5 shows a case of an element with two cut edges. Recall that ghost data is independently set for each cut edge using a unique source point. In this case, an average of the data from all the source points is used as the initial data in the newly uncovered element

$$\rho\left(t^n\right) = \frac{1}{N_{cut}} \sum_{i=1}^{N_{cut}} \rho_{s_i}\left(t^{n-1}\right) \tag{32}$$

$$\mathbf{u}\left(t^n\right) = \frac{1}{N_{cut}} \sum_{i=1}^{N_{cut}} \mathbf{u}_{s_i}\left(t^{n-1}\right) \tag{33}$$

$$p\left(t^n\right) = \frac{1}{N_{cut}} \sum_{i=1}^{N_{cut}} p_{s_i}\left(t^{n-1}\right) \tag{34}$$

where N_{cut} is the number of cut edges in the uncovered element.

3.2. Matching Fluid & Interface Velocities

A necessary condition for the interface conditions, is that they exactly reproduce the limiting case when the interface velocity matches the fluid velocity. In this limiting case, there can be

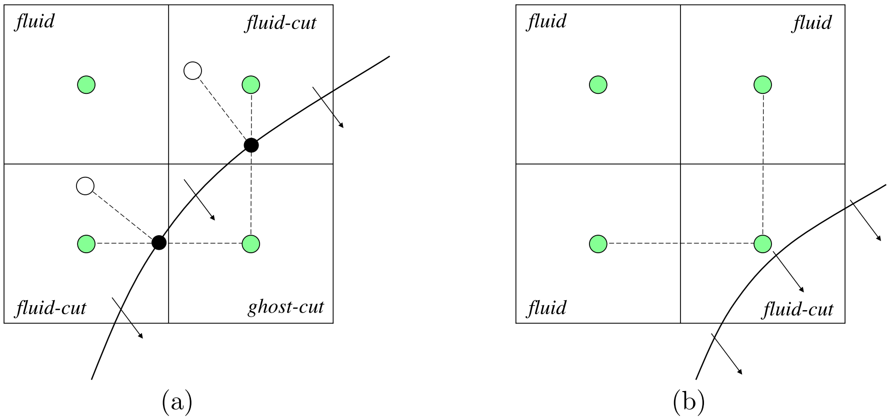

Figure 5. Special case depicting an element with multiple cut edges being uncovered by the interface during a time step. (a) The ghost-cut element at time t^{n-1} has two cut edges each with different source data. (b) An average of all the source data at time t^{n-1} is used as the initial data for the newly uncovered element at time t^n.

no artifacts, i.e., weak shock or rarefactions waves, generated at the interface. This can be verified by an analysis of the numerical flux at an edge cut by an arbitrarily oriented interface.

The numerical flux was presented in part-I [6] as

$$\mathcal{F} \cdot \mathbf{n} = \frac{1}{2} \left\{ (\mathbf{F}(\mathbf{U}_f) + \mathbf{F}(\mathbf{U}_g)) \cdot \mathbf{n} - a(\mathbf{U}_g - \mathbf{U}_f) \right\} \tag{35}$$

where $\mathbf{n}$ is the unit normal to the element face for which the flux is being computed. The subscripts f and g refer to data in the fluid and ghost elements on either side of the cut edge.

The fluid-solid interface conditions were presented in part-I. Applying these conditions at a cut edge gives

$$\begin{gathered} \rho_g = \rho_f \\ \mathbf{u}_g \cdot \mathbf{n}_i = 2(\mathbf{u}_i \cdot \mathbf{n}_i) - \mathbf{u}_f \cdot \mathbf{n}_i \\ \mathbf{u}_g \cdot \mathbf{t}_i = \mathbf{u}_f \cdot \mathbf{t}_i \\ p_g = p_f, \end{gathered} \tag{36}$$

where $\mathbf{n}_i$ and $\mathbf{t}_i$ are the unit normal and tangent vectors to the interface. If the fluid velocity matches the interface velocity, $\mathbf{u}_f = \mathbf{u}_i$, these conditions take the form

$$\begin{gathered} \rho_g = \rho_f \\ \mathbf{u}_g \cdot \mathbf{n}_i = \mathbf{u}_f \cdot \mathbf{n}_i \\ \mathbf{u}_g \cdot \mathbf{t}_i = \mathbf{u}_f \cdot \mathbf{t}_i \\ p_g = p_f. \end{gathered} \tag{37}$$

Substituting these values into the numerical flux function yields zero flux

$$\mathcal{F} \cdot \mathbf{n} = 0 \tag{38}$$

for any cut edge when the fluid velocity matches the interface velocity.

4. COMPARISON OF STATIC AND DYNAMIC INTERFACES

In this section, simulations are presented to verify the implementation of the dynamic interface conditions. Figure 6 shows results for a circular interface moving diagonally across the mesh. The results show that nothing is generated at the boundary and the fluxes are being computed properly for a dynamic interface. The fluid in this problem is taken as air at standard temperature and pressure ($\rho = 1.185\ kg/m^3$, $T = 298\ K$, $p = 1\ atm$). Both the fluid and the interface are given x and y velocity components of $u = v = 600\ m/s$. The computational domain is a $10\ m \times 10\ m$ square.

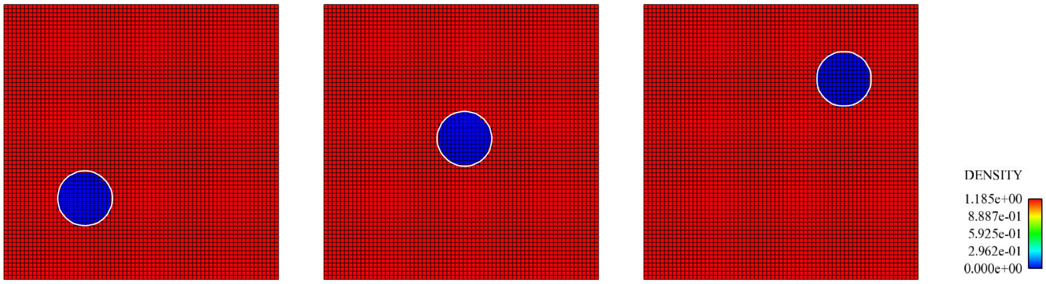

$t = 2.41\ ms$ $t = 6.04\ ms$ $t = 9.66\ ms$

Figure 6. Contour plots of density at three different times with a circular interface moving across the fluid mesh. The interface and fluid have matching velocities. As expected, no flow structures are generated at the interface.

The next problem is adapted from Jiang *et al.* [5]. Here, the same problem is solved in two different reference frames. First, a square projectile is simulated moving through a stationary fluid. Second, the projectile is held fixed, and the fluid is given velocity equal to, but with opposite direction to that of the moving projectile. Solutions are compared at the same time in the simulation to verify both the dynamic interface conditions and the uncovering conditions.

The computational domain for this problem is a $0.65\ m \times 0.2\ m$ rectangle meshed with 130,000 4–node quadrilateral elements. The characteristic element size is 0.001×0.001. The fluid is taken to be air with initial conditions of $\rho = 1.1887\ kg/m^3$, $T = 297\ K$, and $p = 101.3\ kPa$. The rectangular projectile is $0.023\ m \times 0.023\ m$ in size. In the moving projectile case, the projectile has a velocity of Mach 4, or $1382\ m/s$. In the static projectile case, the fluid is given this velocity.

Figures 7 through 10 show comparisons of density, velocity, pressure, and specific internal energy. In each figure, the top half shows results computed with the dynamic interface treatment for the projectile, the bottom half shows results computed for the static projectile. Velocity magnitude is plotted in Figure 8. For a direct velocity comparison, the static results were shifted by the projectile velocity.

Good agreement can be seen in the stand-off and shape of the bow shock in both cases. Some differences can be seen in the contours in the wake. However, results match very well between the two cases showing the dynamic interface conditions and uncovering conditions have been implemented properly.

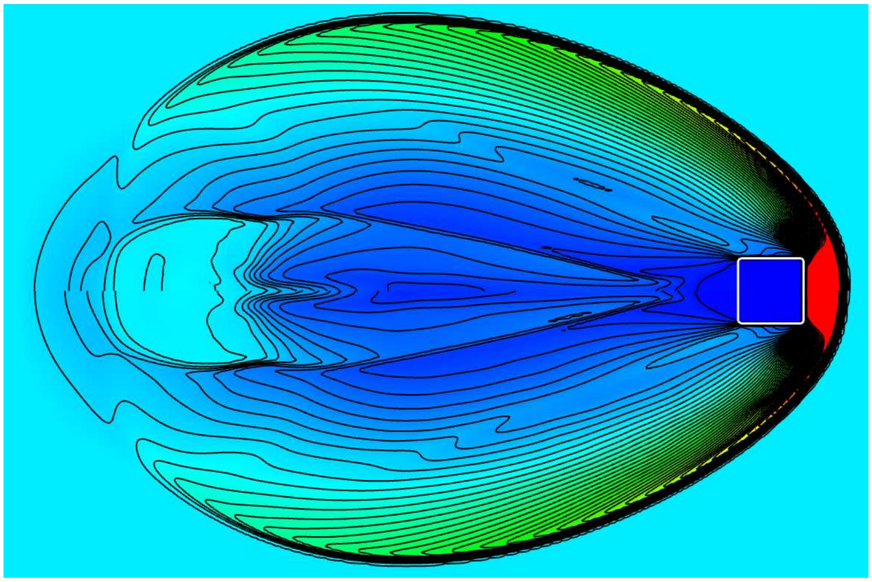

Figure 7. Comparison of density between a static and a dynamic interface. The top half shows results from the dynamic interface. The bottom half shows results for the static interface. Density varies from 0 to 5 kg/m^3 with fifty evenly spaced contours shown.

5. RESULTS

This section presents two and three-dimensional calculations for shock-body interaction problems that involve large bulk rigid-body motion of the fluid-solid interface.

5.1. 2D Projectile from a Shock Tube

We present results for the 2D projectile problem posed by Jiang *et al.* [5]. Here, a square projectile traveling at Mach 4 is ejected from a shock tube. The computational domain used here is similar to that used in [5] and is shown in Figure 11. This domain is meshed with 319,000 4–node quadrilateral elements. The characteristic element size is 0.001×0.001.

The same fluid conditions cited in [5] are used here. The fluid inside the tube is specified as air with initial conditions of $\rho = 5.94\ kg/m^3$, $T = 1723\ K$, $p = 2.94\ MPa$, and $v = 1382\ m/s$. The air outside the tube is given initial conditions of $\rho = 1.19\ kg/m^3$, $T = 297\ K$, $p = 1.01\ MPa$, and $v = 0\ m/s$. The projectile is given a velocity of $v = 1382\ m/s$ to match the fluid velocity inside the tube. The projectile is $0.023\ m \times 0.023\ m$ in size.

Results from the simulation are shown in Figure 12, where density is plotted at various times during the simulation. A shock wave propagates out of the tube ahead of the projectile. A bow shock forms in front of the projectile which interacts with the initial shock from the tube. Eventually, the projectile travels through the shock front that emerged from the tube. The results achieved here match those of Jiang *et al.* very well. However, one difference must be noted. Simulations of Jiang *et al.* account for pressure effects on the projectile. Under pressure,

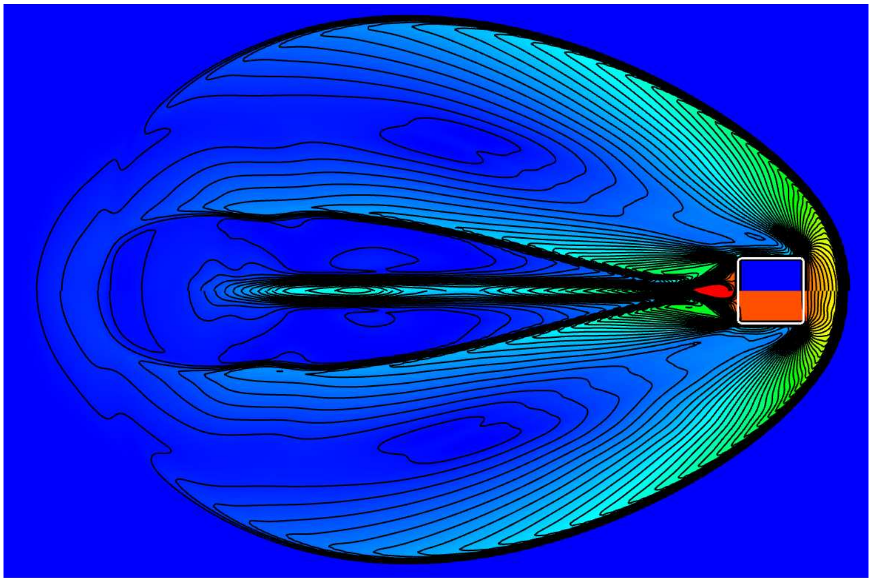

Figure 8. Comparison of velocity between a static and a dynamic interface. The top half shows results from the dynamic interface. The bottom half shows results for the static interface. Velocity varies from 0 to 1500 m/s with fifty evenly spaced contours shown.

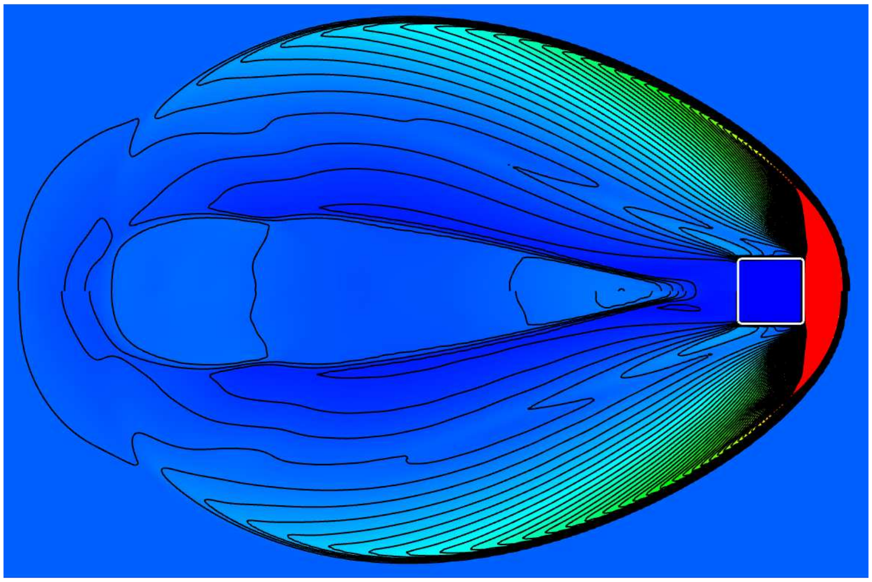

Figure 9. Comparison of pressure between a static and a dynamic interface. The top half shows results from the dynamic interface. The bottom half shows results for the static interface. Pressure varies from 0 to 1 MPa with fifty evenly spaced contours shown.

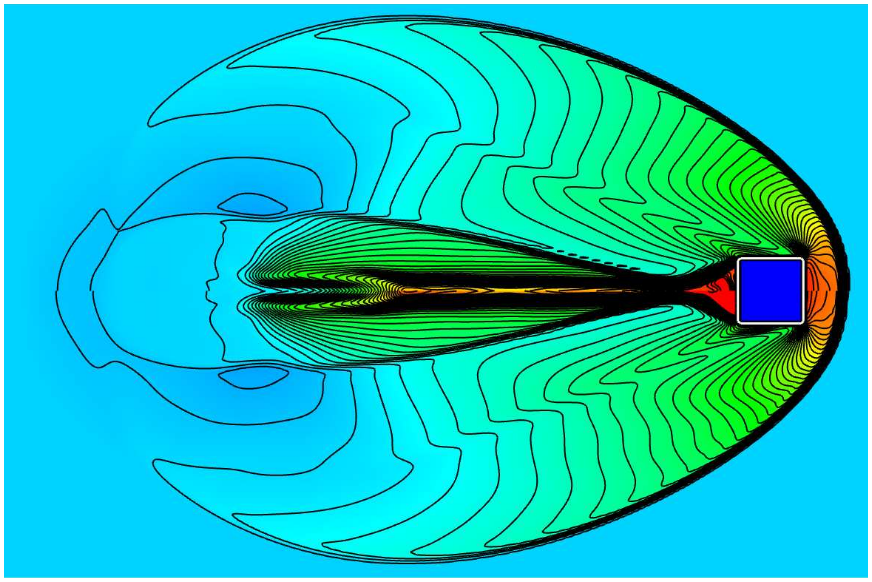

Figure 10. Comparison of internal energy between a static and a dynamic interface. The top half shows results from the dynamic interface. The bottom half shows results for the static interface. Internal energy varies from 0 to 1 MJ/kg with fifty evenly spaced contours shown.

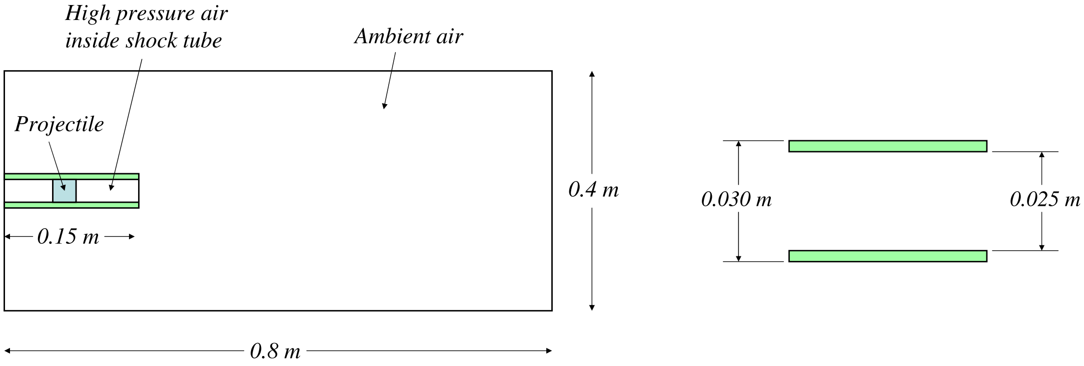

Figure 11. Geometry for the 2D projectile problem. Shown are the overall dimensions and problem setup as well as the shock tube dimensions.

the velocity of the projectile changes over time, unlike here where the projectile velocity is constant. This changes the timing of some of the wave and wave/body interactions. However, even with the absence of these effects, the results here capture the major flow structures.

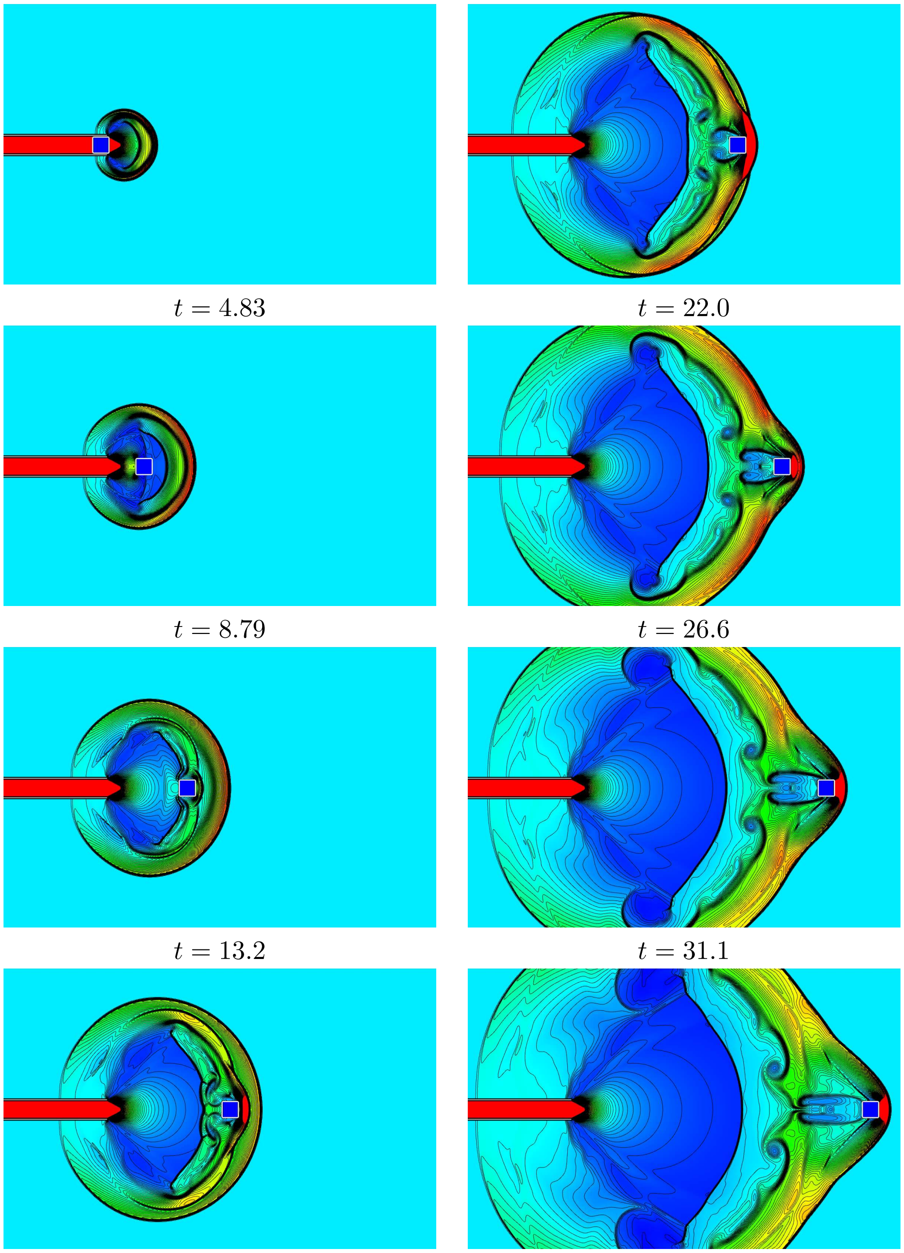

$t = 4.83$ $t = 22.0$

$t = 8.79$ $t = 26.6$

$t = 13.2$ $t = 31.1$

$t = 17.6$ $t = 35.6$

Figure 12. Density contours at various times for the 2D projectile problem. Density varies from 0 to 5 kg/m^3. Fifty contours are plotted over this range every 0.1 kg/m^3. All times are in 10^{-5} seconds.

5.2. 3D Projectile from a Shock Tube

The shock tube problem presented above is extended to three-dimensions with a spherical projectile in a cylindrical shock tube. The initial conditions used in the two-dimensional calculations are used here.

The computational domain used for this problem is shown in Figure 13. The spherical projectile has a diameter of 1.6 m. The domain is meshed with 290,900 8–node hexahedral elements.

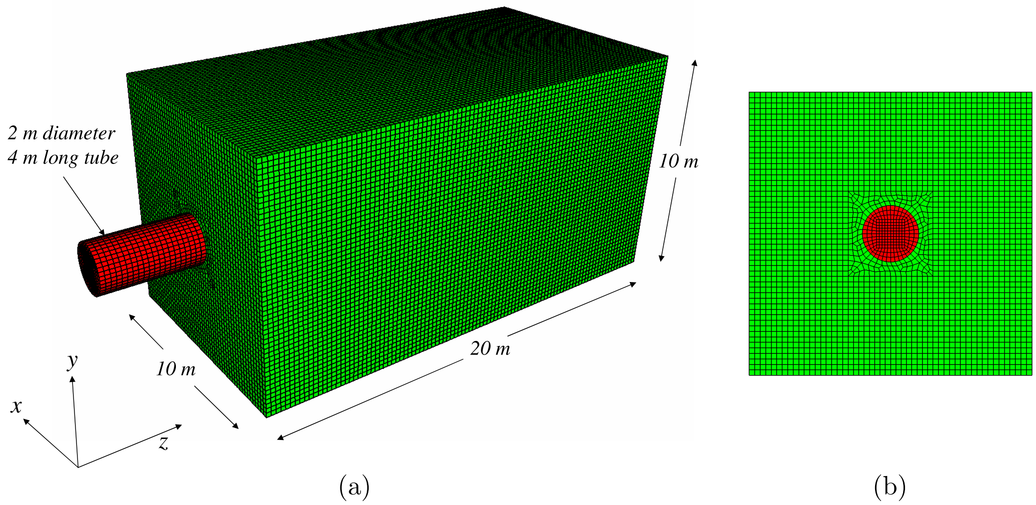

(a) (b)

Figure 13. Domain and mesh for the 3D projectile problem. (a) Isometric view showing entire domain. (b) End view showing the mesh in and around the tube.

Results can be seen in Figure 14. A single isosurface of density with value 2.0 kg/m^3 is plotted within the bounding box of the mesh. The shock waves eventually reach the domain boundaries as can be seen in Figure 14. However, the results are very similar to those presented in §5.1. The major flow structures are captured even on this relatively coarse mesh. An initial shock wave propagates out of the tube. A bow shock forms ahead of the spherical projectile which catches up and passes through the initial shock wave from the tube.

5.3. Shock Wave Impacting a Moving Sphere

This section presents results for a Mach 3 shock wave impacting a translating sphere. The sphere also has a velocity of Mach 3. The computational domain for this problem is an 11 $m \times 10\ m \times 10\ m$ rectangle meshed with 1,100,000 8–node hexahedral elements. The fluid is taken as air with initial conditions and inlet conditions as specified in Figure 15. The sphere has a diameter of 2.0 m and a velocity of 1038 m/s. The sphere travels diagonally (corner-to-corner) across the domain.

Results are plotted in Figure 16 at various times throughout the simulation. In the figure, a single isosurface of density with value 2.0 kg/m^3 is shown within the bounding box of the

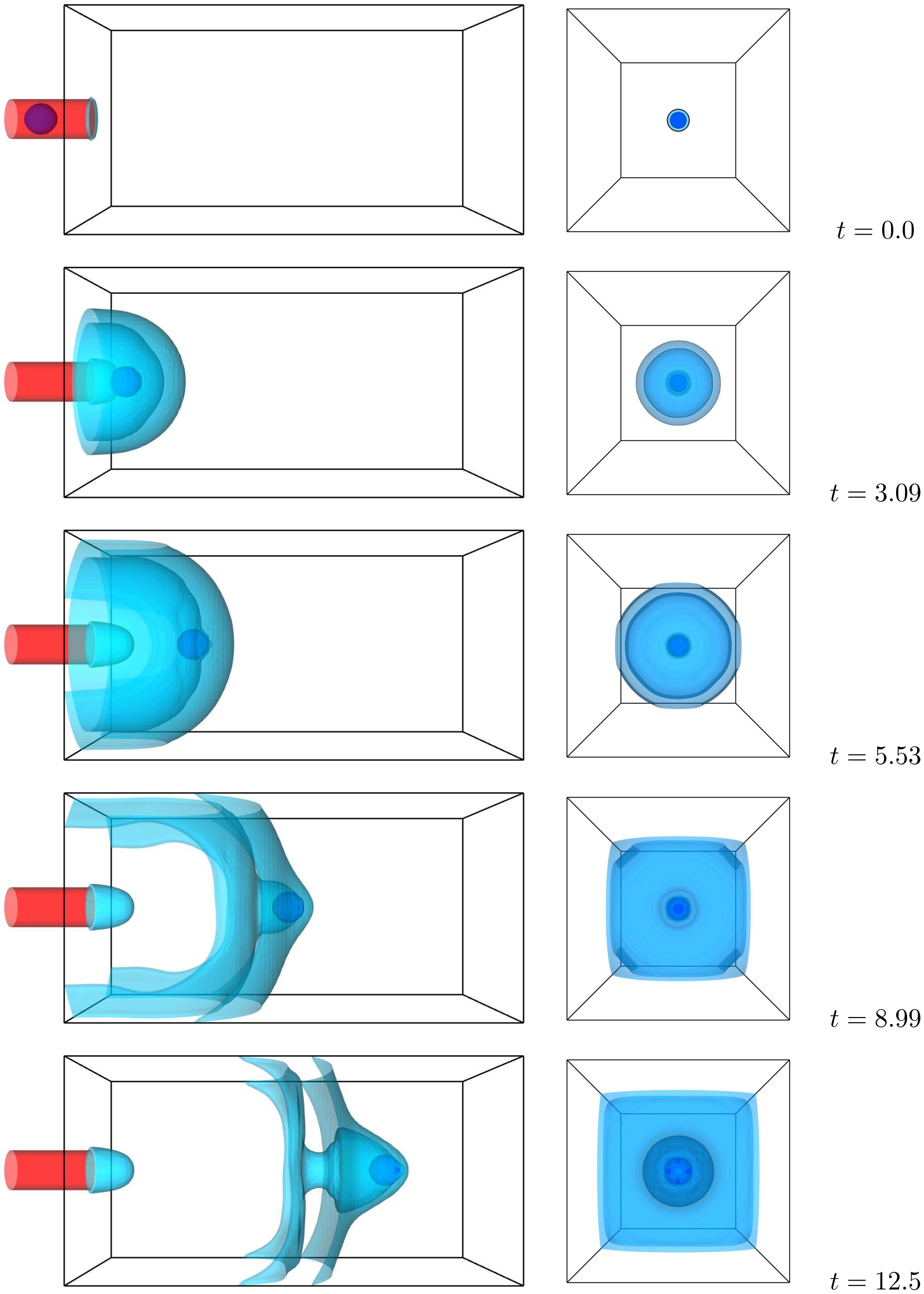

Figure 14. Density at various times for the 3D projectile problem. One isosurface of density is plotted at a value of 2.0 kg/m^3. All times are in ms.

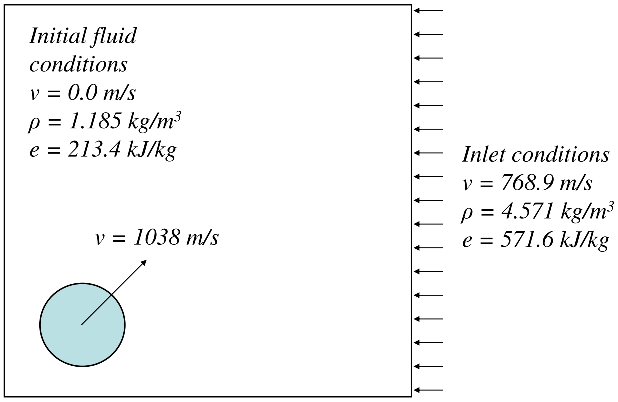

Figure 15. Problem setup for a shock wave impacting a spherical projectile.

domain. A bow shock forms around the sphere as it moves through the fluid. The incoming shock wave interacts with this bow shock as it passes over the sphere.

Again, a fairly coarse mesh has been used for this problem due to computer resource limitations. However the major flow structures such as the bow shock in front of the sphere and the incoming shock wave have been captured. Additionally, in these types of three-dimensional flows, large density and pressure gradients exist across each of the shocks. Vorticity is generated where these gradients do not align. Isosurfaces of helicity are plotted in Figure 17. Two counter rotating structures develop as the two shock waves interact. These isosurfaces are stretched and pulled along in the wake of the plane shock and the sphere.

Unfortunately, no similar results, experimental or analytical, are available for a direct comparison at this time. However, this simulation highlights the type of problems that the interface schemes presented here are able to address. This problem is considered another successful test of the dynamic interface conditions in three-dimensions with complex shock/body interactions.

6. SUMMARY & CONCLUSIONS

In this work, the methods developed in [7] and [6] have been extended to treat the dynamic interfaces in FSI problems where the solid experiences large bulk Lagrangian displacements. A monolithic explicit time-integration method for the fully-coupled fluid-solid system has been introduced and applied to problems where the solid exhibits translational motion. The extensions for the moving interface, construction of state data associated with the "uncovering" conditions were developed, and the overall approach verified by considering problems where the translational velocity of the solid matched the convective velocity of the fluid. A series of computations have demonstrated that the combination of the super-sampled $\mathcal{L}^2$ projection for fast-level set construction, narrow-band method for finding source data, and uncovering

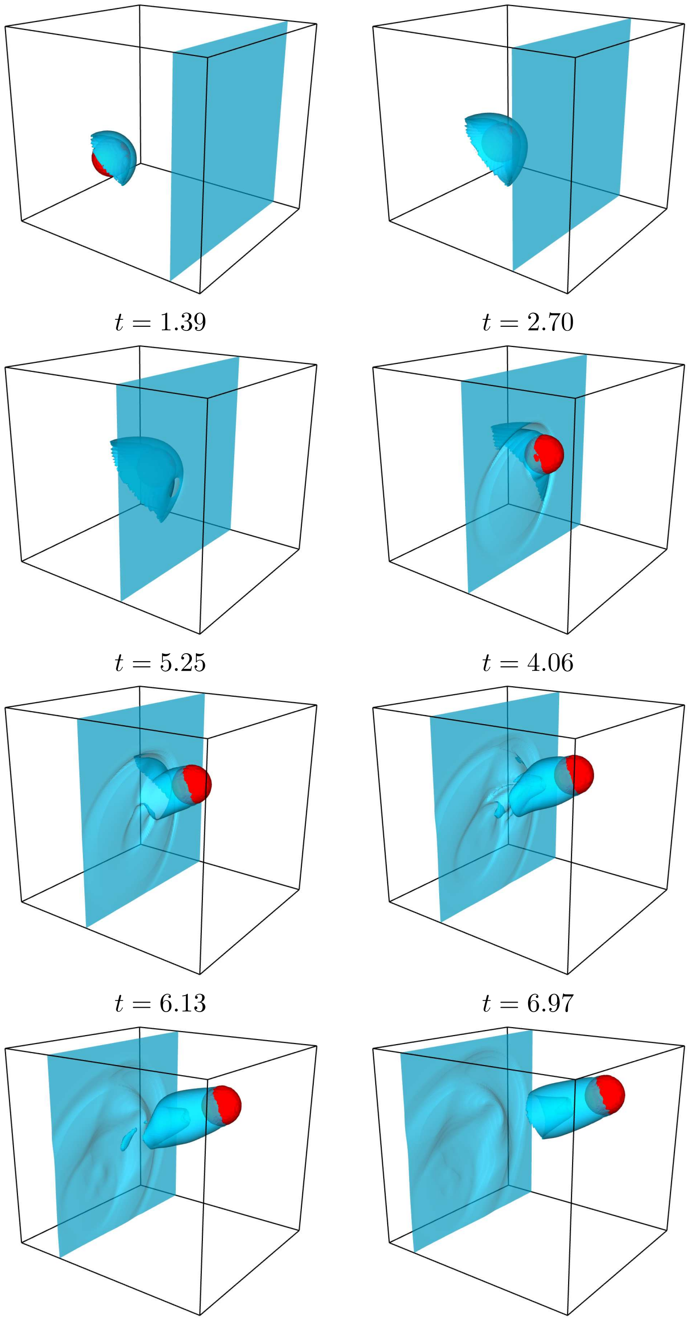

$t = 1.39$ $t = 2.70$

$t = 5.25$ $t = 4.06$

$t = 6.13$ $t = 6.97$

$t = 7.84$ $t = 8.74$

Figure 16. Density at various times for a shock wave impacting a spherical projectile. One isosurface of density is plotted at a value of 2.0 kg/m^3. All times are in ms.

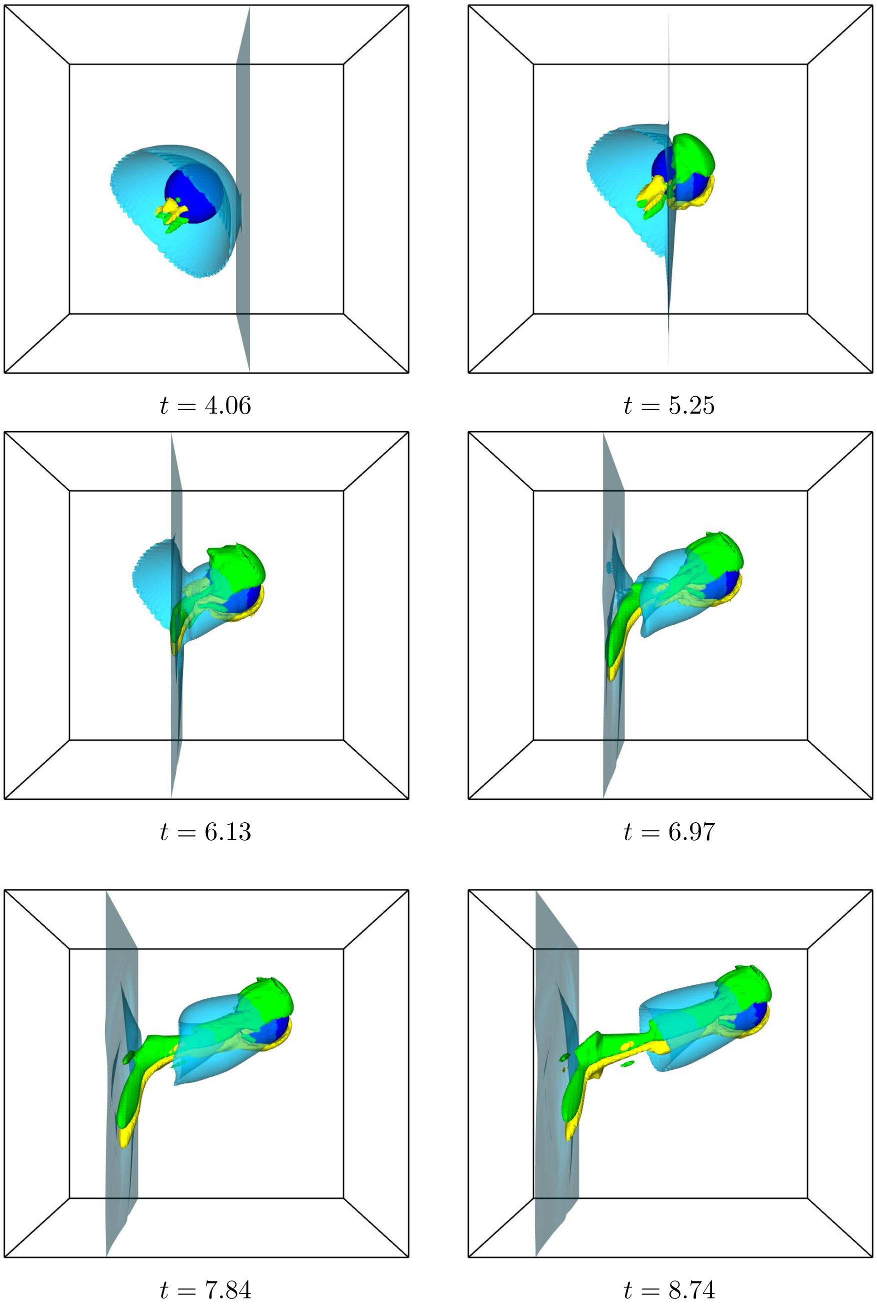

$t = 4.06$ $t = 5.25$

$t = 6.13$ $t = 6.97$

$t = 7.84$ $t = 8.74$

Figure 17. Helicity at various times for a shock wave impacting a spherical projectile. Two isosurfaces of helicity are plotted at $\pm 5.0 \times 10^4$ m/s^2. All times are in ms.

conditions is computationally efficient for a broad set of FSI problems where shock-wave loading is important.

ACKNOWLEDGEMENTS

This work was supported by Sandia National Laboratories and the ASC hydro methods effort at Los Alamos National Laboratory. Sandia is a multiprogram laboratory operated by Sandia Corporation, a Lockheed Martin Company, for the United States Department of Energy's National Nuclear Security Administration under contract DE-AC04-94AL85000.

REFERENCES

1. F. M. L. Amirouche, *Computational Methods in Multibody Dynamics*, Prentice-Hall, Inc., 1992.
2. D. Baraff, *An introduction to physically based modeling: Rigid body simulation I - unconstrained rigid body dynamics*, tech. rep., Robotics Institute, Carnegie Mellon University, 1997.
3. S. Gottlieb and C.-W. Shu, *Total variation diminishing Runge–Kutta schemes*, Mathematics of Computation, 67 (1998), pp. 73–85.
4. S. Gottlieb, C.-W. Shu, and E. Tadmor, *Strong stability–preserving high–order time discretization methods*, SIAM Review, 43 (2001), pp. 89–112.
5. Z. Jiang, K. Takayama, and B. W. Skews, *Numerical study on blast flowfields induced by supersonic projectiles discharged from shock tubes*, Physics of Fluids, 10 (1998), pp. 277–288.
6. D. G. Tipton, M. A. Christon, and M. S. Ingber, *Coupled fluid-solid interaction under shock wave loading: part-I – static interfaces*, submitted to International Journal for Numerical Methods in Fluids, (2007).
7. ———, *A super-sampled projection method for level-set construction in fluid-solid interaction problems*, submitted to International Journal for Numerical Methods in Fluids, (2009).